Liu, Z., et al., 2023, Mantle serpentinization and associated hydrogen flux at North Atlantic magma-poor rifted margins: Geology, https://doi.org/10.1130/G50722.1

Mantle Serpentinisation and Associated Hydrogen Flux at North Atlantic Magma-poor Rifted Margins

Zhonglan Liu, Marta Gussinyer Perez*, Javier García-Pintado, Leila Mezri and Wolfgang Bach

This PDF file includes:

S1: Model Approach

Governing equations

We use a finite element code to solve the equations of mass, momentum, and energy conservation branched from MILAMIN (Dabrowski et al., 2008). The model includes a dynamic topography by using a stress-free surface (Andrés-Martinez et al., 2015), and has previously been used to investigate geological problems such as melting and serpentinisation (Ros et al., 2017), feedback from surface processes (i.e., erosion and sedimentation) on the architecture and evolution of passive margins (Andrés-Martínez et al., 2019), and sedimentation and unconformity patterns at continental margins during rifting and breakup (Pérez-Gussinyé et al., 2020). Deformation and pressure are calculated by solving Stokes force-balance equation:

$$\nabla \cdot \tau - \nabla \mathrm{P} + \rho g = 0 \tag{S1}$$

where τ is deviatoric stress, P the total pressure, ρ the density and g the gravitational acceleration, and mass conservation equation:

$$\nabla \cdot v = 0 \tag{S2}$$

where v is velocity. Temperature is estimated by solving the energy conservation equation:

$$\rho C_P \cdot \frac{DT}{Dt} = \nabla \cdot (k \nabla T) + H_0 + H_S \tag{S3}$$

where C_P is the effective heat capacity, T is the temperature, t is the time, k is the thermal conductivity, H_0 is the crustal radioactive heat production, and H_S is the shear heating production that depends on

stress and strain rate. To consider the cooling effects of seawater circulation, we increase the thermal conductivity, *k,* in the areas where faults and fractures are assumed to bring water into the basement:

$$k = \begin{cases} Nu \cdot k_0 & Z < 6\ km\ and\ T < 600\ ºC \\ k_0 & Z \geq 6\ km\ or\ T \geq 600\ ºC \end{cases} \quad \text{(S4)}$$

where Z is the depth below seafloor and T is temperature, Nu is a dimensionless quantity, which we assume to take the value of 8 in our reference model, and k_0 is the base thermal conductivity.

Rock Rheology models

Visco-elasto-plastic rheology is achieved by adopting an additive decomposition of the deviatoric strain rate into elastic, viscous, and plastic components. The relation between shear stress τ and effective viscosity η_{eff} described as:

$$\tau = \eta_{eff} \cdot 2\dot{\varepsilon} \quad \text{(S5)}$$

where $\dot{\varepsilon}$ the deviatoric strain rate.

The Drucker-Prager yield equation is adopted to evaluate whether the material deforms plastically or visco-elastically. Plastic deformation dominates the model when the second invariant of deviatoric stress σ_{II} , is larger than the plastic yield stress σ_{yield}, which is defined as:

$$\sigma_{yield} = P\ sin\varphi + C\ cos\varphi \quad \text{(S6)}$$

where C is the cohesion of the rocks and φ is the friction angle. To include plasticity into the viscous formulation, the effective viscosity η_{eff} of yielding material is defined as:

$$\eta_{eff} = \frac{\sigma_{yield}}{2\dot{\varepsilon}_{II}} \quad \text{(S7)}$$

where $\dot{\varepsilon}_{II}$ is the square root of the second invariant of strain rate. When $\sigma_{\mathrm{II}} < \sigma_{yield}$, the material behaves visco-elastically, and we describe effective viscosity η_{eff} as:

$$\frac{1}{\eta_{eff}} = \left(\frac{1}{\eta_{dis}} + \frac{1}{\eta_{dif}} + \frac{1}{\mu\Delta t}\right) \tag{S8}$$

where η_{dis} is the dislocation creep viscosity, η_{dif} is the diffusion creep viscosity, μ is the shear modulus and Δt is the numerical time step. The creep flow is described by nonlinear power-law temperature- and stress-dependent rheologies as:

$$\eta_{dis/dif} = \mathrm{B}^{-\frac{1}{n}}\dot{\varepsilon}_{II}^{\frac{1-n}{n}} exp\left(\frac{E + PV}{nRT}\right) \tag{S9}$$

where *B* is the pre-exponential factor of the flow law, n is the power-law exponent, *E* is the activation energy, *V* is the activation volume, *R* is the gas constant, and *T* is the absolute temperature.

Weakening mechanisms

Both plastic and viscous strain softening are introduced to help localize deformation. The friction angle of 30° (friction coefficient of 0.577) is linearly reduced to 15° (friction coefficient of 0.268) with the accumulated plastic strain increased from 0 to 1. When increasing the viscous accumulated strain from 0 to 1, the pre-exponential factor B of the dislocation creep law (Eq. S8) linearly increases from 1 to 30. The abundance of serpentine in the major fault zones (Blackman et al., 2002) indicates that it has a lower mechanical strength than unaltered ultramafic rocks. This view is consistent with laboratory experiments on serpentine gouges (Escartin et al., 2001; Tesei et al., 2018).

To mimic the effect of serpentinization-induced weakening, the friction angle was further decreased linearly from 15 degrees to 5 degrees with $D_{serp} \cdot \varepsilon_p$ increasing from 0 to 0.1(Fig. S1c).

Surface process

The erosion- sedimentation process is achieved by assuming that the rate of surface elevation change is equal to the sediment flux plus a source term (e.g., Olive et al., 2014; Anders-Martinez et al., 2019):

$$\frac{\partial h}{\partial t} = \frac{\partial}{\partial x}(K\frac{\partial h}{\partial x}) + C_S \quad \text{(S10)}$$

where h is the surface elevation, K is the diffusivity, x is the horizontal direction and C_S is an additional pelagic sediment source.

K varies depending on whether the surface is above sea-level or not. When sediments are subaerial, K is described as:

$$K = K_L + kax_d \quad \text{(S11)}$$

where K_L is the subaerial diffusion coefficient, α is the coefficient of transport and x_d is the distance from topographic highs to drainage divide.

When sediments are in submarine conditions, K is determined as:

$$K = K_s e^{(-\lambda_s h_w)} \quad \text{(S12)}$$

where K_S is the submarine diffusion coefficient, λ_s is the submarine diffusion decay coefficient and h_w is the water depth. The surface-process parameters used in the models are shown in Table S1.

S2: Model Setup

We consider an initial 150 km wide and 80 km deep model (*Fig S1*). A half extension rate is applied as the velocity boundary condition at the right and left sides of the model. We applied a Winkler boundary condition for the bottom boundary, which means that the pressure is equal along the model bottom during the model run (Poliakov and Buck, 1998). This is equivalent to assuming that extension of the model box is overlying an inviscid fluid.

The initial crustal thickness is set to 30 km, supported by seismic data onshore Iberia (Zelt et al., 2003). The initial Moho temperature is varied by changing the lower crust radiogenic heat production. Pressure-temperature-time (P-T-t) paths of amphibolite from site 1067 ODP drilling (Gardien et al., 2001) give a range of temperatures of 550-770 ºC for the pre-rift Moho. Previous studies (e.g. (Buck, 1991; Ros et al., 2017)) showed that with initial Moho temperatures > 650 ºC, flat Moho is expected due to the low viscosity of the lower crust, which does not match the unlulatiing Moho structure observed in seismic sections (e.g., (Osmundsen and Péron-Pinvidic, 2018; Pérez-Gussinyé et al., 2003)), and that when the initial Moho temperature is low, the model forms a symmetric conjugate structure, which is not consistent with observations from North Atlantic rifted margins (Fig 1). Here, following previous modelling studies ((Brune et al., 2014; Liu et al., 2021)), we use 600 ºC as the initial Moho temperature, which allows for producing the observed the margin structure.

The rheology of the crust is considered to be one of the important factors controlling rift evolution (e.g., (Ros et al., 2017)). In this paper, we assume that the rheological properties of the crust are wet anorthite ((Rybacki and Dresen, 2000) Table S1). Using wet anorthite instead of wet quartzite

(Gleason and Tullis, 1995) allows for a certain strength of the lower crust during deformation. The main evidence for such a setting is the following: 1) Seismic studies of the Galicia Interior Basin, west of Iberia (e.g., Pérez-Gussinyé et al., 2003), indicating a P-wave velocity in the lower crust of > 6.6 km/s and therefore suggesting the existence of strong mafic lower crust. 2) A recent work ((Dunkel et al., 2021)) reported textures indicative of seismic faulting in lower crustal rocks from the Northern Norwegian Caledonides reveal very high stress levels thus suggesting that the lower crust is very strong rather than weak during deformation. 3) Studies from the Alpine Tethys system also demonstrate the existence of lower crustal gabbros there ((Manatschal et al., 2007)). 4) The work coupling upper crustal fault geometry and forward geodynamic modelling (Liu et al., 2022) showed that the observed rifted margin structure from the West Iberian margin can be reproduced only when a strong crust is used.

One can also expect that if a weaker crust (e.g., wet quartzite) is used, the width of the margin will be wider compared to the model shown in Figure 2, but this does not really affect the mantle exhumation and serpentinization at COTs and development of COTs, where the continental crust has already been broken up.

References in appendix

Andrés-Martínez, M., Morgan, J. P., Pérez-Gussinyé, M., & Rüpke, L. (2015). A new free-surface stabilization algorithm for geodynamical modelling: Theory and numerical tests.Physics of the Earth and Planetary Interiors,246, 41–51. https://doi.org/10.1016/j.pepi.2015.07.003

Andrés‐Martínez, M., Pérez-Gussinyé, M., Armitage, J., and Morgan, J. P., 2019, Thermomechanical Implications of Sediment Transport for the Architecture and Evolution of Continental Rifts and Margins: Tectonics, v. 38, no. 2, p. 641-665.

Blackman, D. K., Karson, J. A., Kelley, D. S., Cann, J. R., Früh-Green, G. L., Gee, J. S., Hurst, S. D., John, B. E., Morgan, J., and Nooner, S. L., 2002, Geology of the Atlantis Massif (Mid-

Atlantic Ridge, 30 N): Implications for the evolution of an ultramafic oceanic core complex: Marine Geophysical Researches, v. 23, no. 5, p. 443-469.

Brune, S., Heine, C., Pérez-Gussinyé, M., and Sobolev, S. V., 2014, Rift migration explains continental margin asymmetry and crustal hyper-extension: Nature Communications, v. 5, p. 4014.

Buck, W. R., 1991, Modes of continental lithospheric extension: Journal of Geophysical Research, v. 96, no. B12, p. 20161-20178.

Dunkel, K. G., Zhong, X., Arnestad, P. F., Valen, L. V., and Jamtveit, B., 2021, High transient stress in the lower crust: Evidence from dry pseudotachylytes in granulites, Lofoten Archipelago, northern Norway: Geology, v. 49, no. 2, p. 135-139.

Dabrowski, M., Krotkiewski, M., and Schmid, D., 2008, MILAMIN: MATLAB ‐based finite element method solver for large problems: Geochemistry, Geophysics, Geosystems, v. 9, no. 4.

Escartin, J., Hirth, G., and Evans, B., 2001, Strength of slightly serpentinized peridotites: Implications for the tectonics of oceanic lithosphere: Geology, v. 29, no. 11, p. 1023-1026.

Gardien, V., Poupeau, G., Muceku, B., Hébert, R., Beaudoin, G., and Labrin, E., 2001, The evolution of amphibolites from Site 1067, ODP Leg 173 (Iberia Abyssal Plain): Jurassic rifting to the Pyrenean compression: Geological Society, London, Special Publications, v. 187, no. 1, p. 191-208.

Gleason, G. C., and Tullis, J., 1995, A flow law for dislocation creep of quartz aggregates determined with the molten salt cell: Tectonophysics, v. 247, no. 1-4, p. 1-23.

Liu, z., Pérez-Gussinyé, M., Rüpke, L., Muldashev, I., Minshull, T. A., and Bayrakci, G., 2021, Lateral coexistence of ductile and brittle deformation shapes magma-poor margins: Earth and Planetary Science Letters.

Manatschal, G., Müntener, O., Lavier, L., Minshull, T., and Péron-Pinvidic, G., 2007, Observations from the Alpine Tethys and Iberia–Newfoundland margins pertinent to the interpretation of continental breakup: Geological Society, London, Special Publications, v. 282, no. 1, p. 291-324.

Osmundsen, P., and Péron-Pinvidic, G., 2018, Crustal-scale fault interaction at rifted margins and the formation of domain-bounding breakaway complexes: Insights from offshore Norway: Tectonics, v. 37, no. 3, p. 935-964.

Pérez-Gussinyé, M., Ranero, C. R., Reston, T. J., and Sawyer, D., 2003, Mechanisms of extension at nonvolcanic margins: Evidence from the Galicia interior basin, west of Iberia: Journal of Geophysical Research: Solid Earth, v. 108, no. B5.

Poliakov, A. N., and Buck, W. R., 1998, Mechanics of stretching elastic-plastic-viscous layers: Applications to slow-spreading mid-ocean ridges: Faulting and magmatism at mid-ocean ridges, p. 305-323.

Ros, E., Pérez-Gussinyé, M., Araújo, M., Romeiro, M. T., Andrés-Martínez, M., and Morgan, J. P., 2017, Lower Crustal Strength Controls on Melting and Serpentinization at Magma-Poor Margins: Potential Implications for the South Atlantic: Geochemistry Geophysics Geosystems, no. 1.

Rybacki, E., and Dresen, G., 2000, Dislocation and diffusion creep of synthetic anorthite aggregates: Journal of Geophysical Research: Solid Earth, v. 105, no. B11, p. 26017-26036.

Tesei, T., Harbord, C., De Paola, N., Collettini, C., and Viti, C., 2018, Friction of mineralogically controlled serpentinites and implications for fault weakness: Journal of Geophysical Research: Solid Earth, v. 123, no. 8, p. 6976-6991.

Zelt, C. A., Sain, K., Naumenko, J. V., and Sawyer, D. S., 2003, Assessment of crustal velocity models using seismic refraction and reflection tomography: Geophysical Journal International, v. 153, no. 3, p. 609-626.

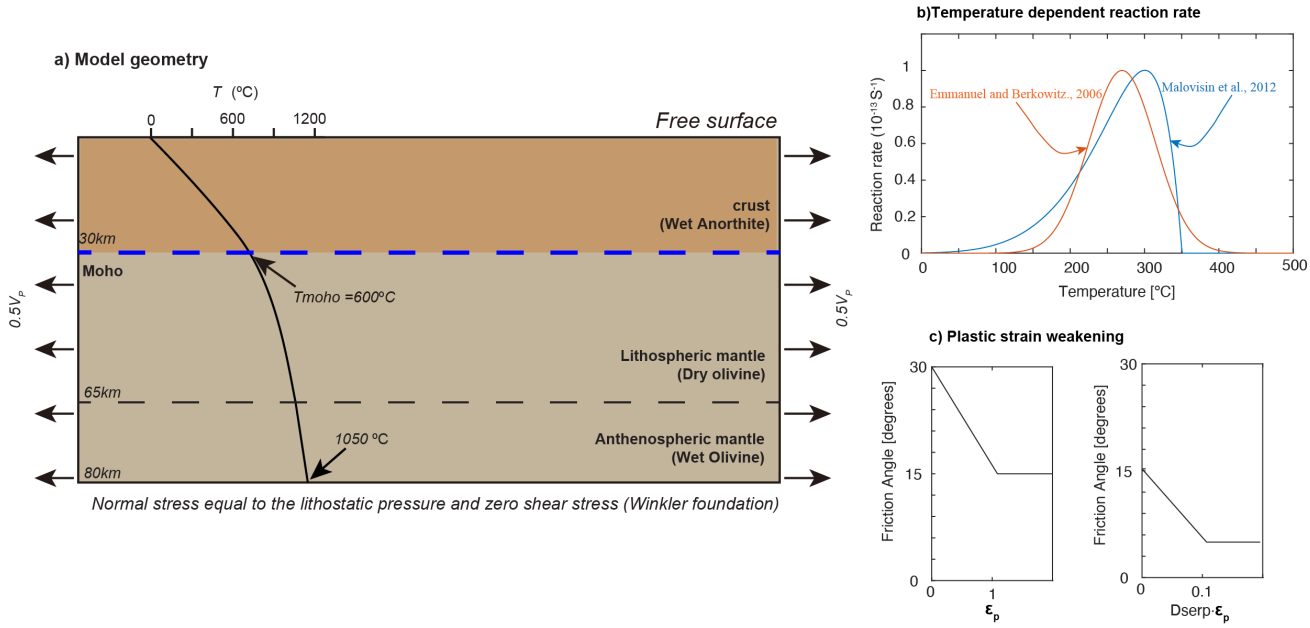

Figure S1. Model setup. (a) Model geometry, the Moho temperature is regulated by crustal radiative heat. To localize extension at the start of the model, a temperature anomaly of 100 ºC is added to our model at Moho depth. This allows the deformation to be localized to several major faults in a relatively short numerical time. (b)Two temperature-dependent serpentinization rates follow previous work by Emmanuel and Berkowitz., 2006 and Malovision et al., 2012. (c) The model includes plastic strain weakening from 30 º to 15º, left panel. In addition, to mimic the effect of serpentinization-induced weakening, the friction angle, which had already been reduced by the plastic strain weakening, was further reduced linearly from 15º to 5 º, with $D_{serp} \cdot \varepsilon_p$ increasing from 0 to 0.1. Thus, this effect will be larger with an increasing degree of serpentinization.

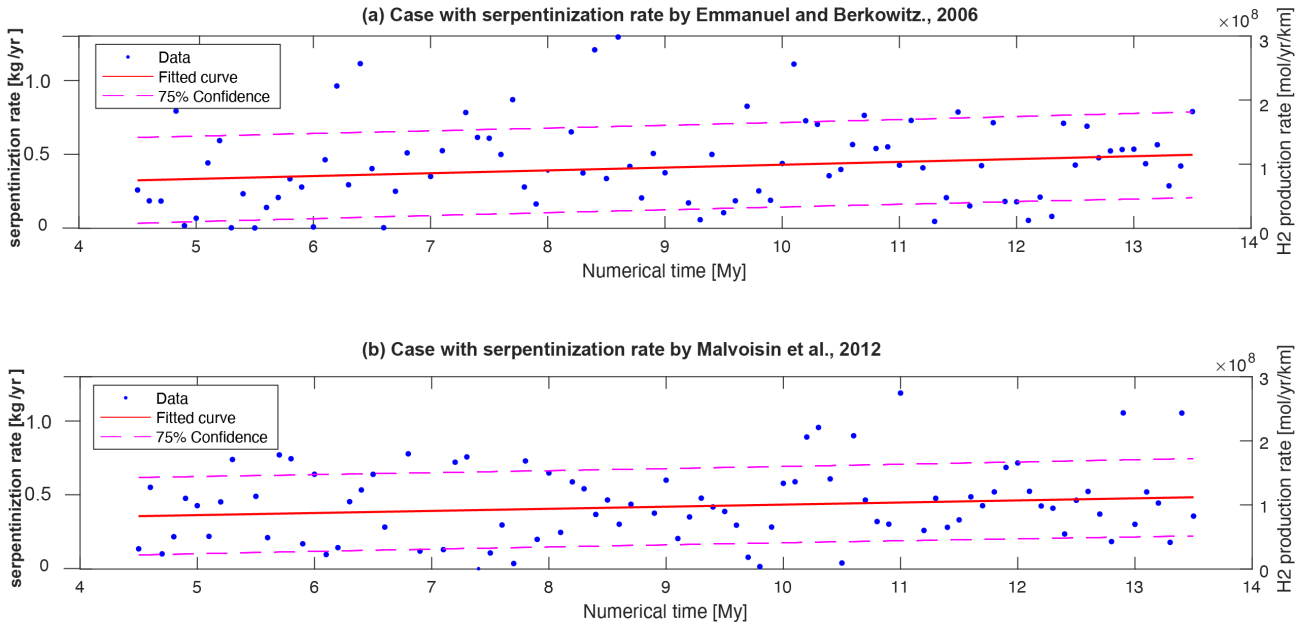

Figure S2. Modelled H2 production rate with two different temperature-dependent function for serpentinization. (a) The H2 production rate with numerical simulation time with kinetic function provided by Emmanuel and Berkowitz., 2006. (b) The H2 production rate with numerical simulation time with kinetic function provided by Malvoisin et al., 2012. The case (b) with the Malvoisin et al., 2012 kinetic function has an average H_2 production rate of ~ $8.3 \cdot 10^7$ mol/yr per kilometer along the rift, which is slightly higher than ~ $7.5 \cdot 10^7$ mol/yr for case (a), but the difference is small, especially compared to the effect of extension rate and hydrothermal cooling (Figure 3).

Table S1. Model parameters.

Thermomechanical parameters			
Variable [unit]	Wet Anorthite	Dry Olivine	Wet Olivine
Dislocation pre-exponential factor $\log(B_{dis})$ [Pa^{-n} S^{-1}]	-15.4	-15.96	-15.81
Dislocation exponent n_{dis}	3.0	3.5	3.5
Dislocation activation energy E_{dis} [kJ/mol]	356	530	480
Dislocation activation volume V_{dis} [10^{-6} m^3/mol]	-	13	10
Diffusion pre-exponential factor $\log(B_{dif})$ [Pa^{-n} S^{-1}]	-	-8.16	-8.64
Diffusion exponent n_{dif}	-	1	1
Diffusion activation energy E_{dif} [kJ/mol]	-	375	335
Diffusion activation volume V_{dif} [10^{-6} m^3/mol]	-	6	4
Shear Modulus μ [GPa]	40	74	74
Thermal conductivity K [Wm^{-1} K^{-1}]	2.5	3.3	3.3
Heat capacity C_P [J kg^{-1} K^{-1}]	1200	1200	1200
Radiogenic heat production H_r [μWm^{-3}]	0.2	0	0
Bulk density ρ [kg m^{-3}]	2850	3300	3300
Thermal expansivity coefficient α [10^{-5} K^{-1}]	2.4	3.0	3.0
Initial cohesion (MPa)	10	10	10
Initial friction angle (°)	30	30	30
Surface process parameters			
Subaerial hillslope diffusion, K_L [m^2/year]	0.25		
Subaerial discharge transport coefficient α	$5 \cdot 10^{-4}$		
Submarine diffusion coefficient, Ks [m^2/year]	10^2		
Submarine diffusion coefficient decay, λ_s [m^{-1}]	$5 \cdot 10^{-4}$		
Pelagic sediment rate, C_S [m/year]	10^{-5}		

L: Labrador- WG: West Greenland margins

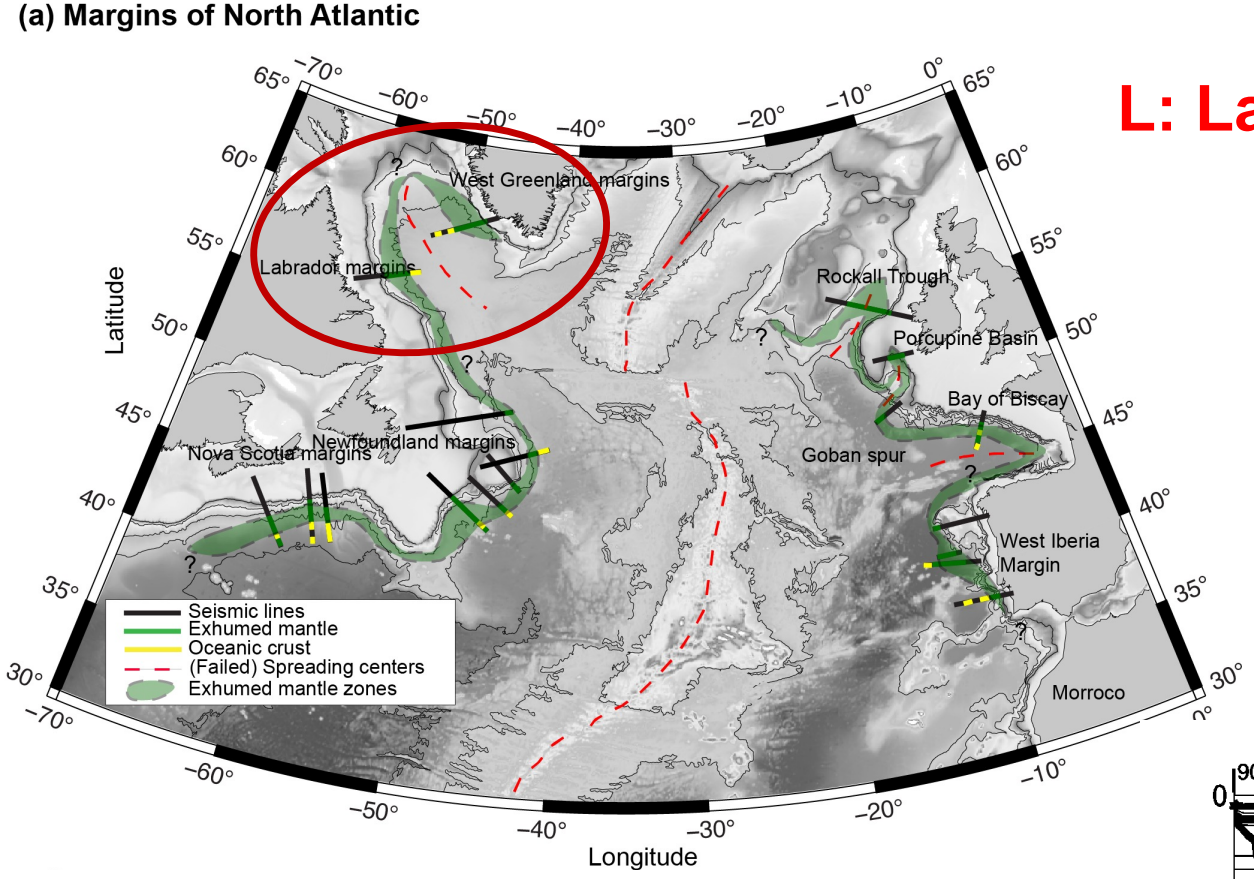

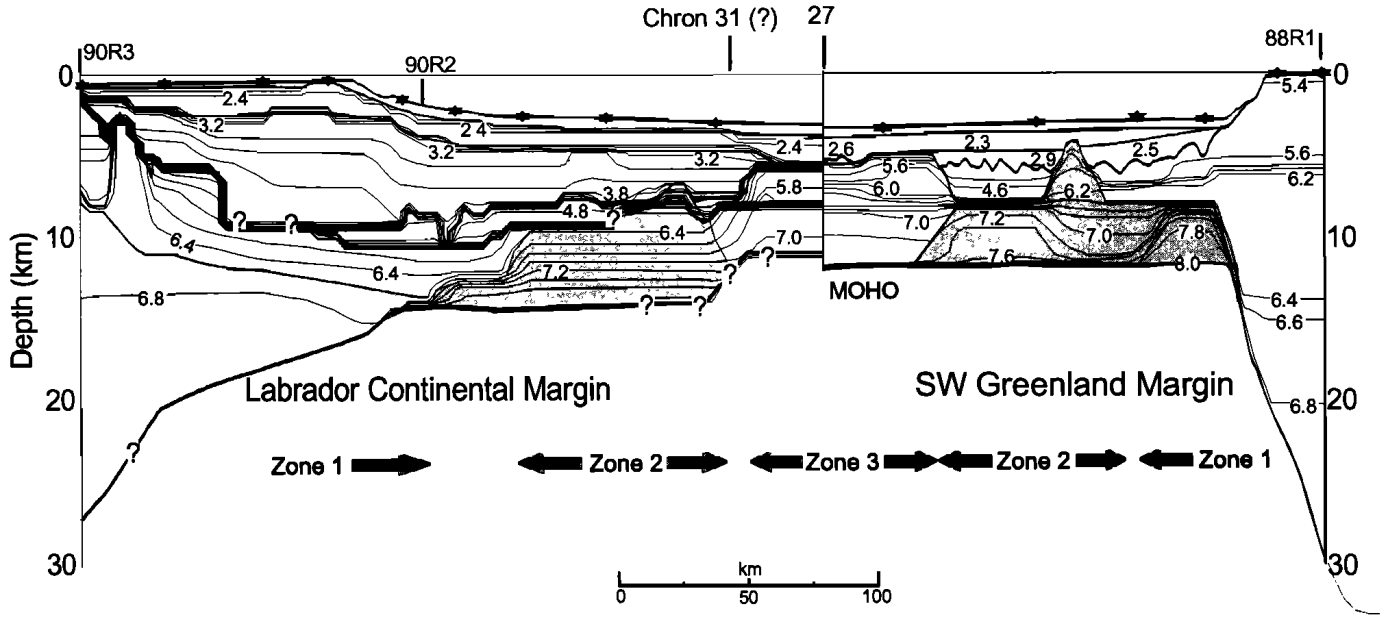

Chian, D., Louden, K. E., & Reid, I. (1995). Crustal structure of the Labrador Sea conjugate margin and implications for the formation of nonvolcanic continental margins. Journal of Geophysical Research: Solid Earth, 100(B12), 24239-24253.

Liu, Z., et al., 2023, Mantle serpentinization and associated hydrogen flux at North Atlantic magma-poor rifted margins: Geology, https://doi.org/10.1130/G50722.1

Orphan Basin

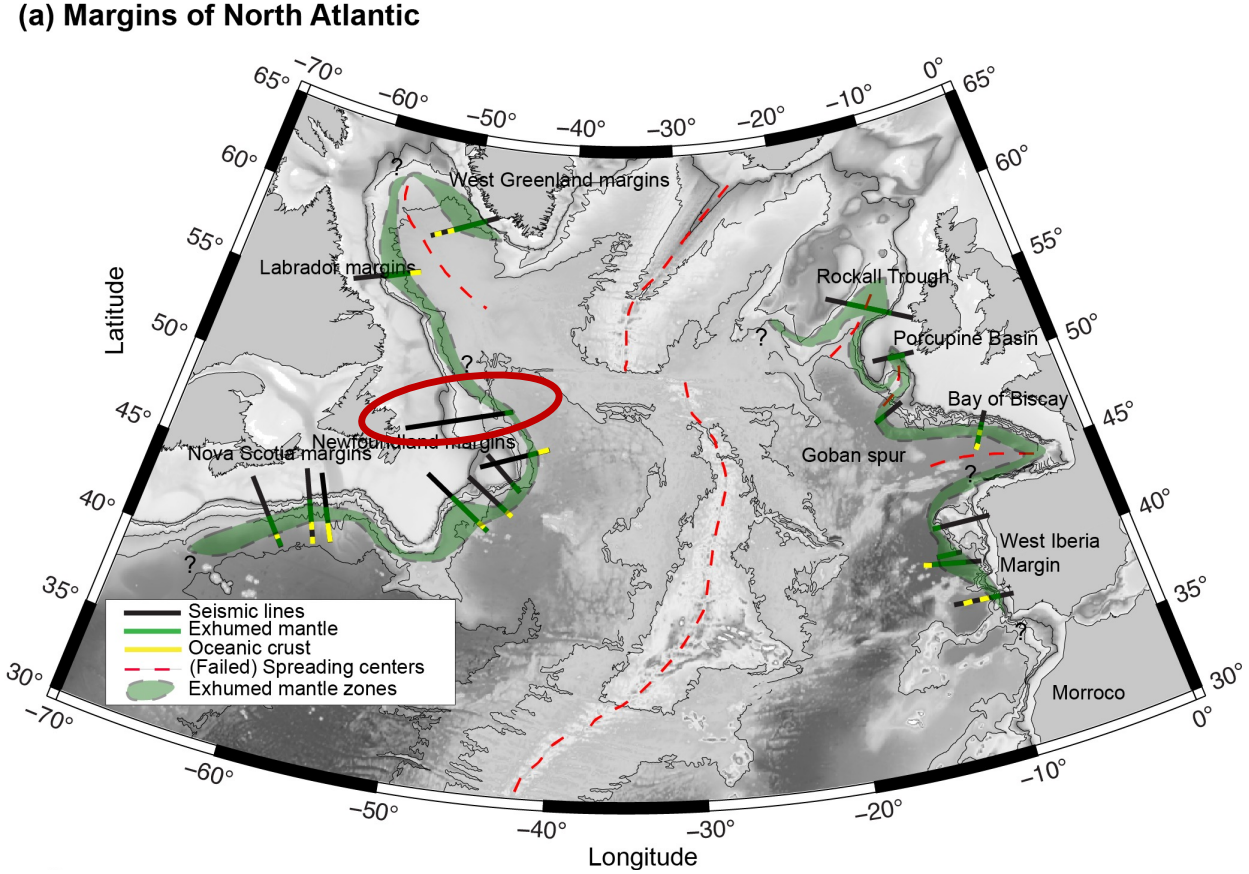

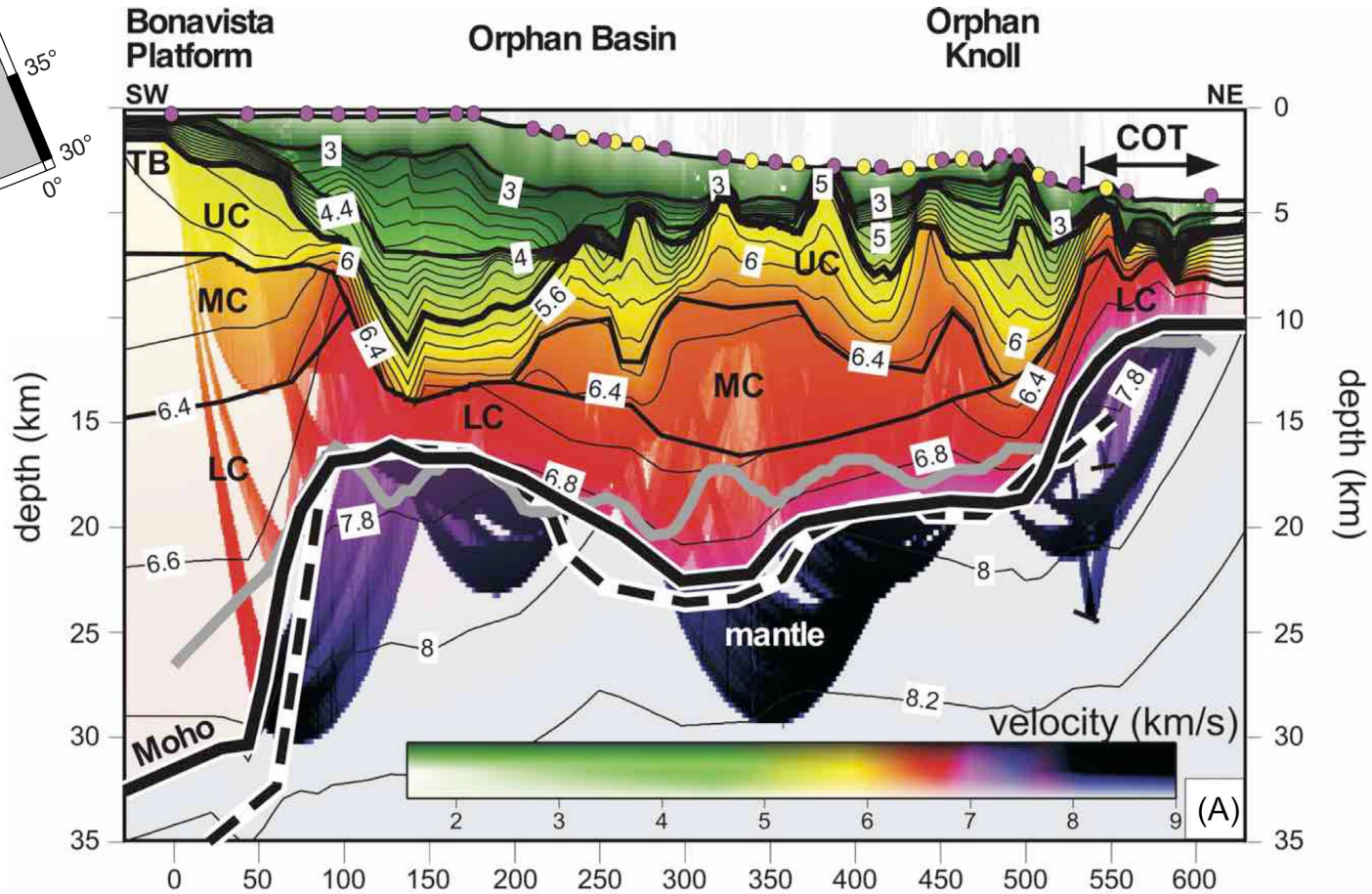

Welford, J. K., Dehler, S. A., and Funck, T., 2020, Crustal velocity structure across the Orphan Basin and Orphan Knoll to the continent–ocean transition, offshore Newfoundland, Canada: Geophysical Journal International, v. 221, no. 1, p. 37-59.

(a) Margins of North Atlantic

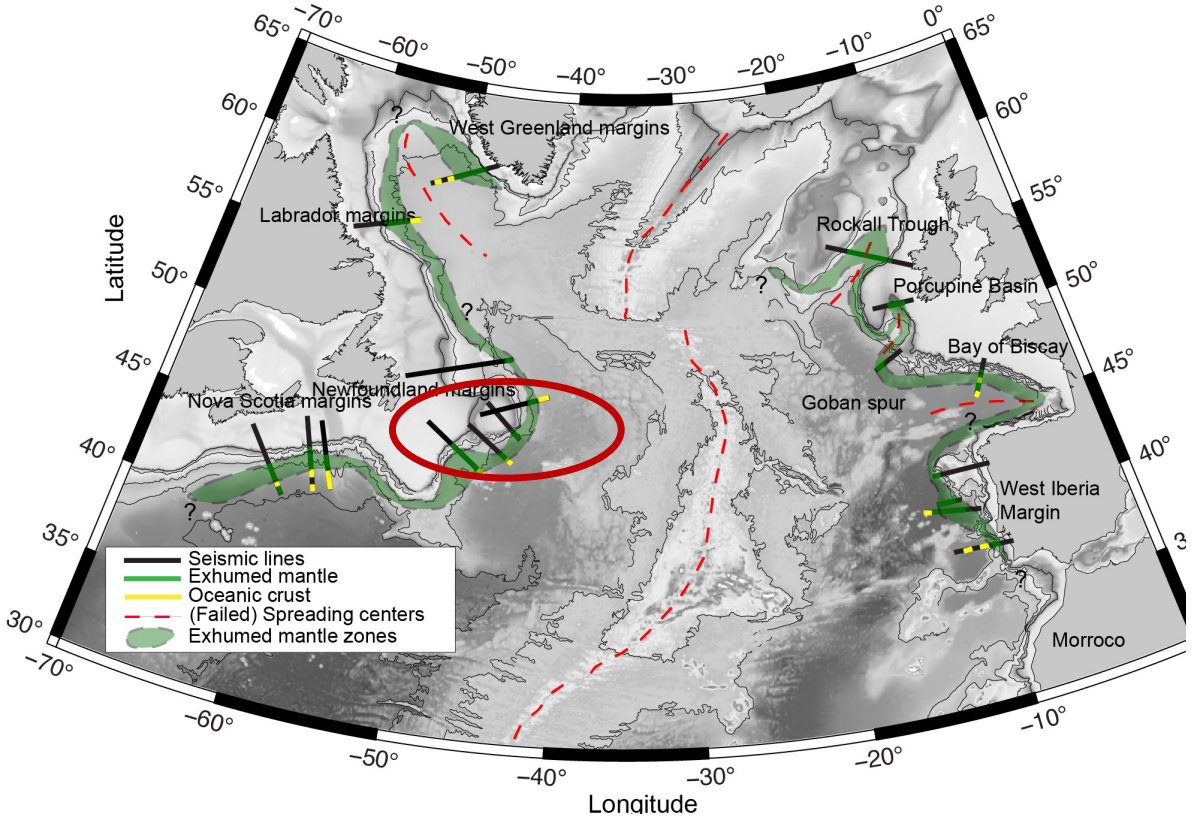

Newfoundland Margin

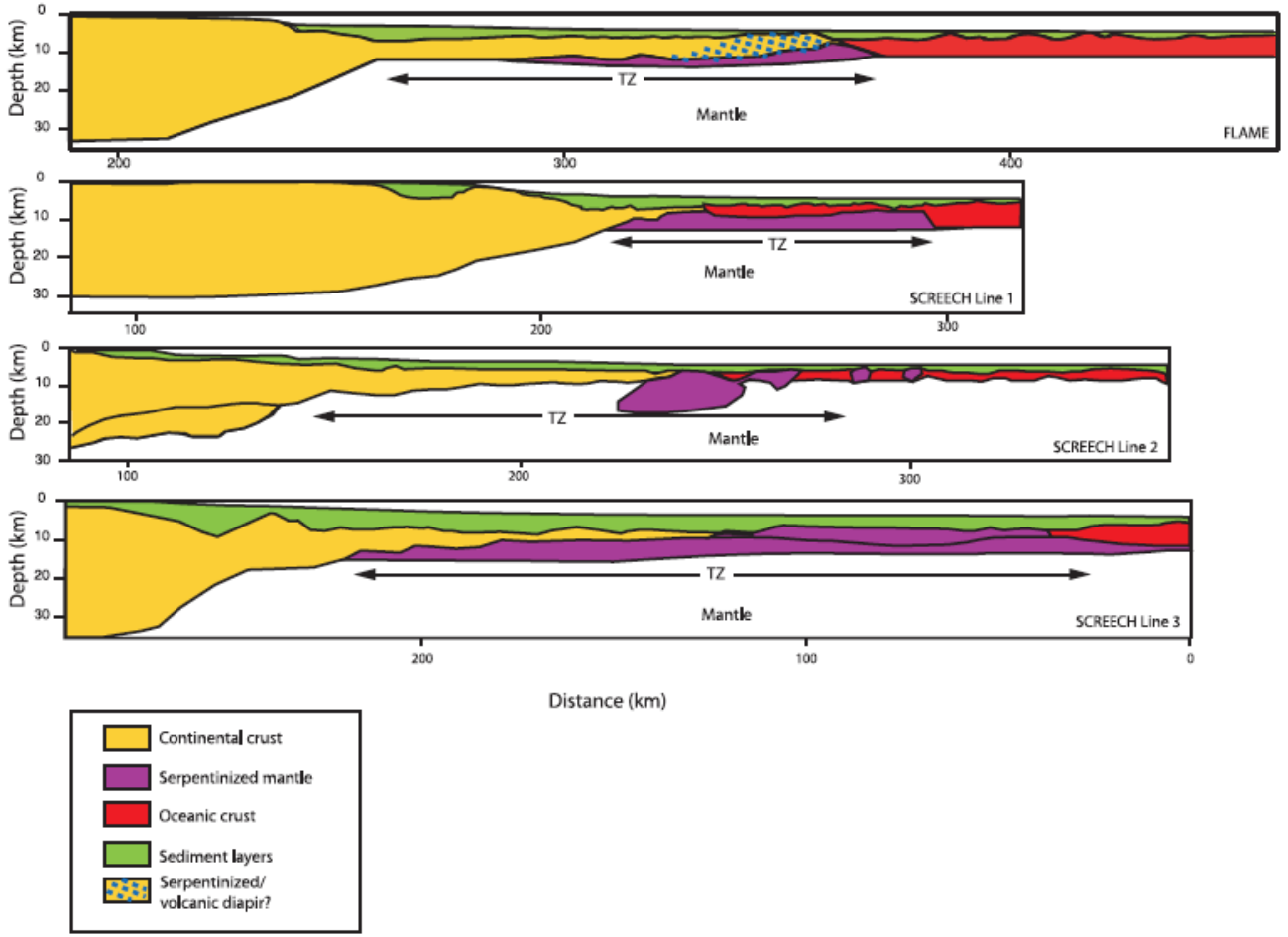

Gerlings, J., Louden, K. E., and Jackson, H. R., 2011, Crustal structure of the Flemish Cap Continental Margin (eastern Canada): an analysis of a seismic refraction profile: Geophysical Journal International, v. 185, no. 1, p. 30-48.

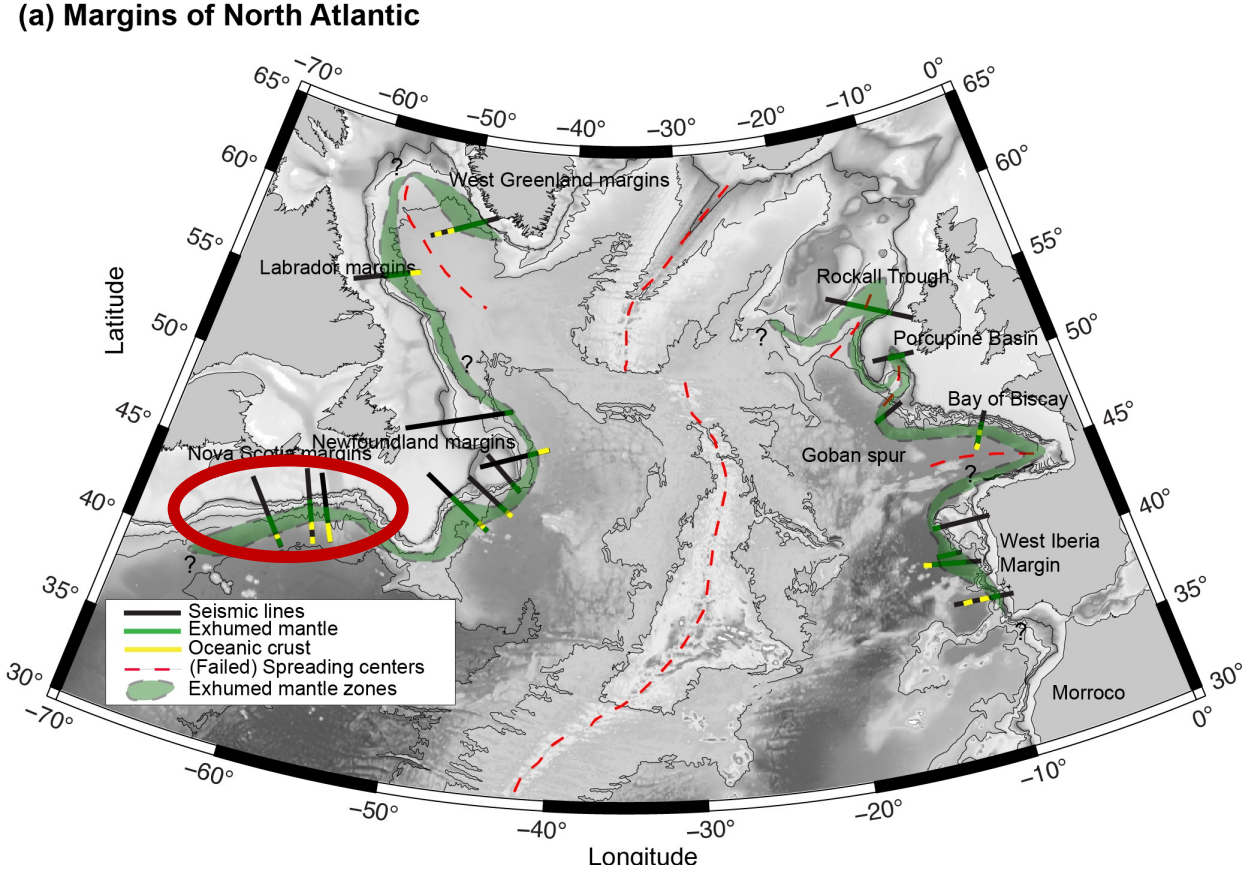

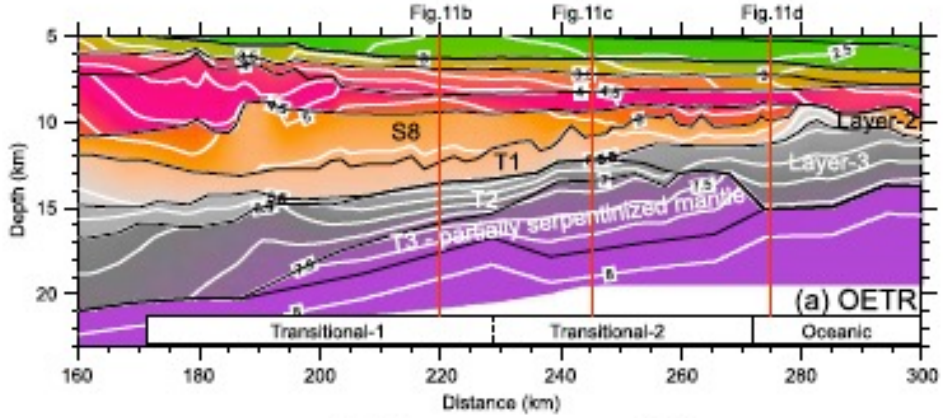

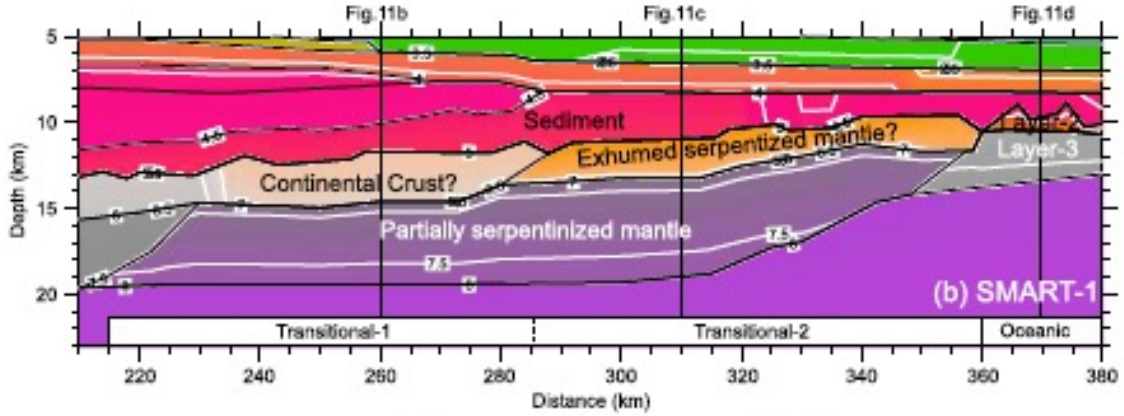

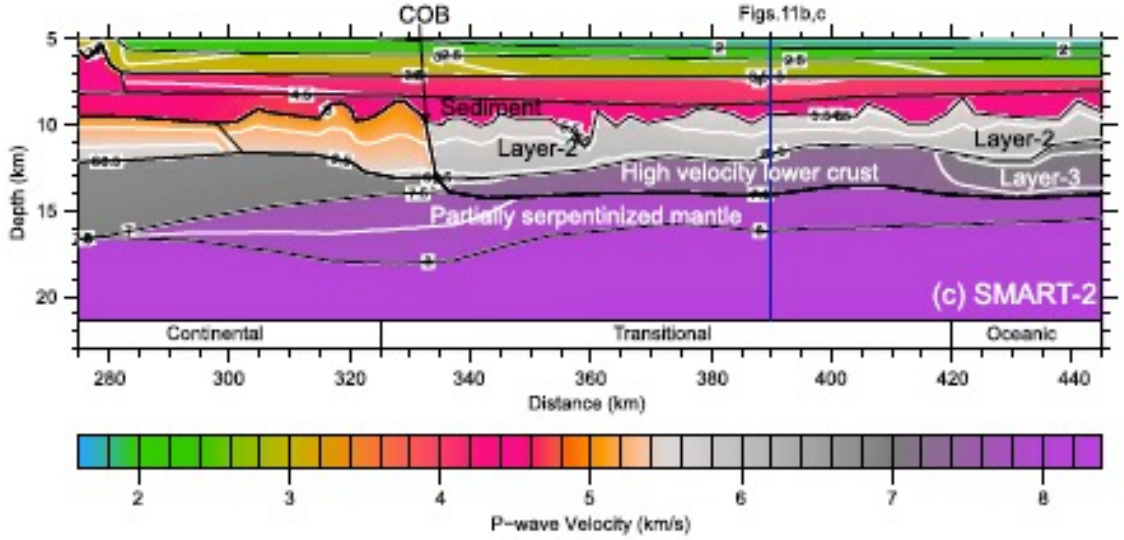

Nova Scotia

Jian, H., Nedimović, M. R., Canales, J. P., & Lau, K. H. (2021). New Insights Into the Rift to Drift Transition Across the Northeastern Nova Scotian Margin From Wide‐Angle Seismic Waveform Inversion and Reflection Imaging. Journal of Geophysical Research: Solid Earth, 126(12), e2021JB022201.

Rockall Trough

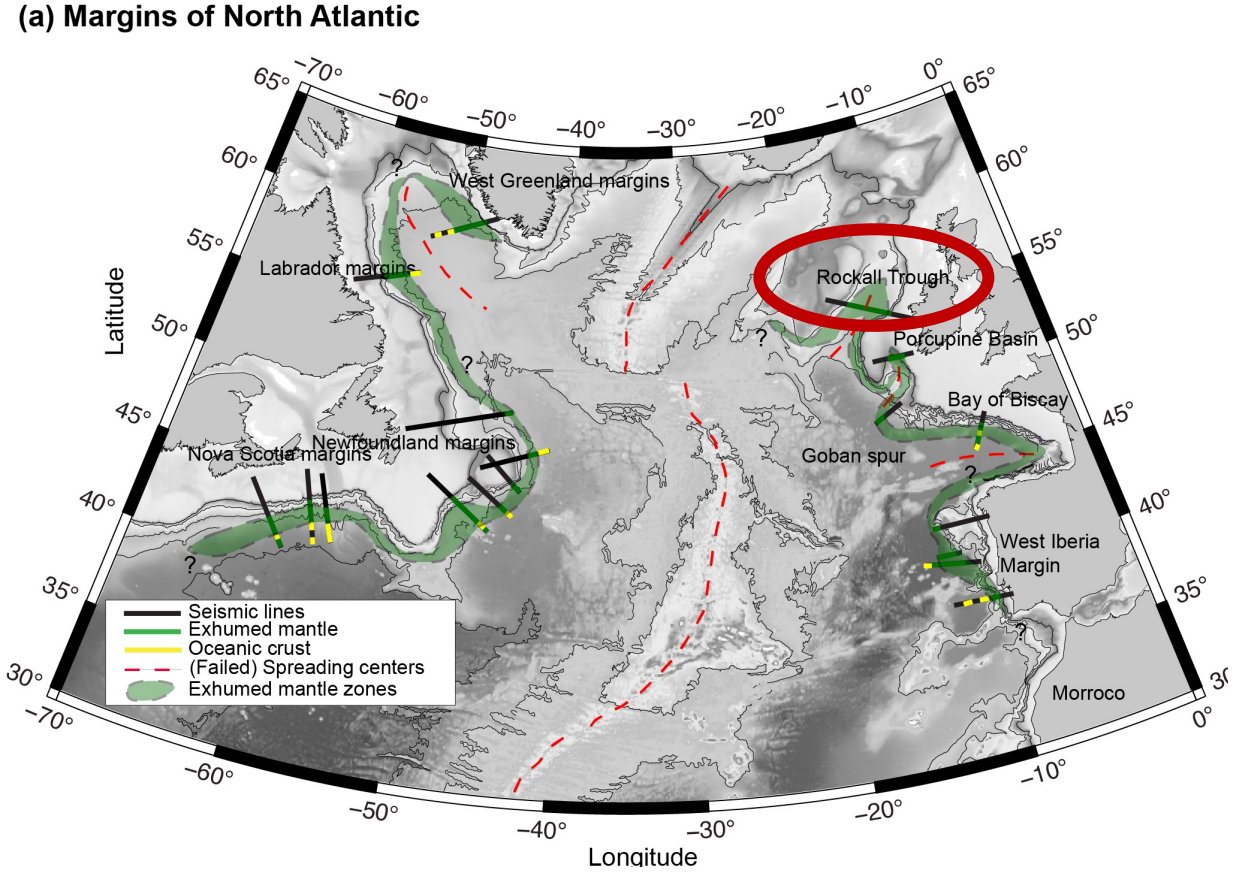

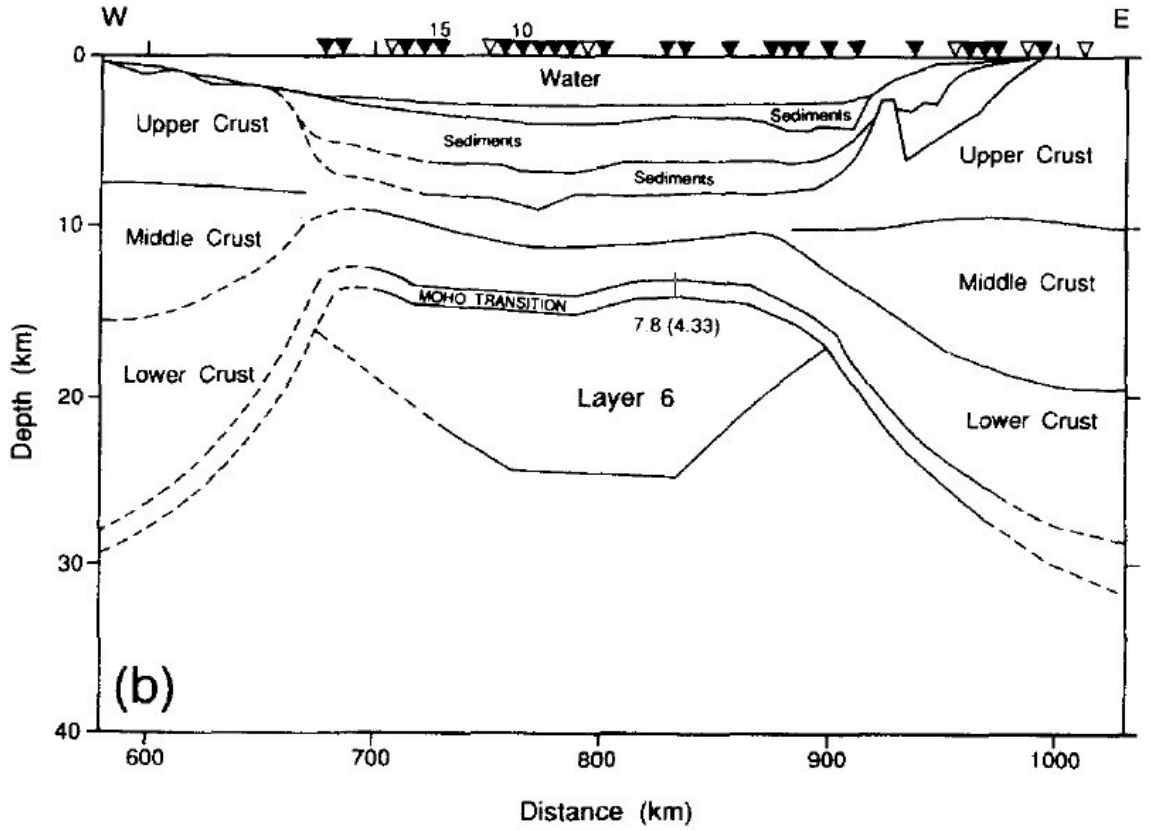

O'Reilly B M, Hauser F, Jacob A W B, et al. The lithosphere below the Rockall Trough: wide-angle seismic evidence for extensive serpentinisation. Tectonophysics, 1996, 255(1-2): 1-23.

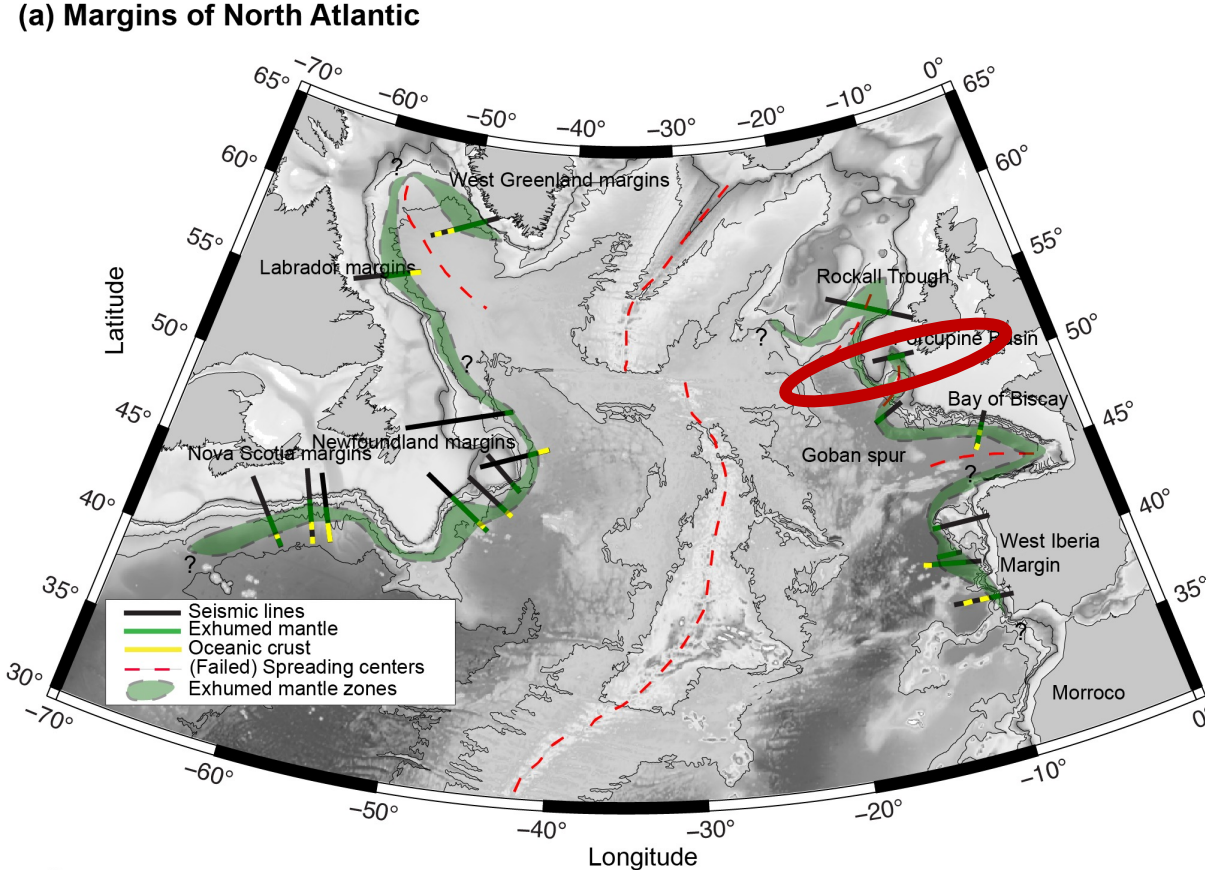

Porcupine Basin

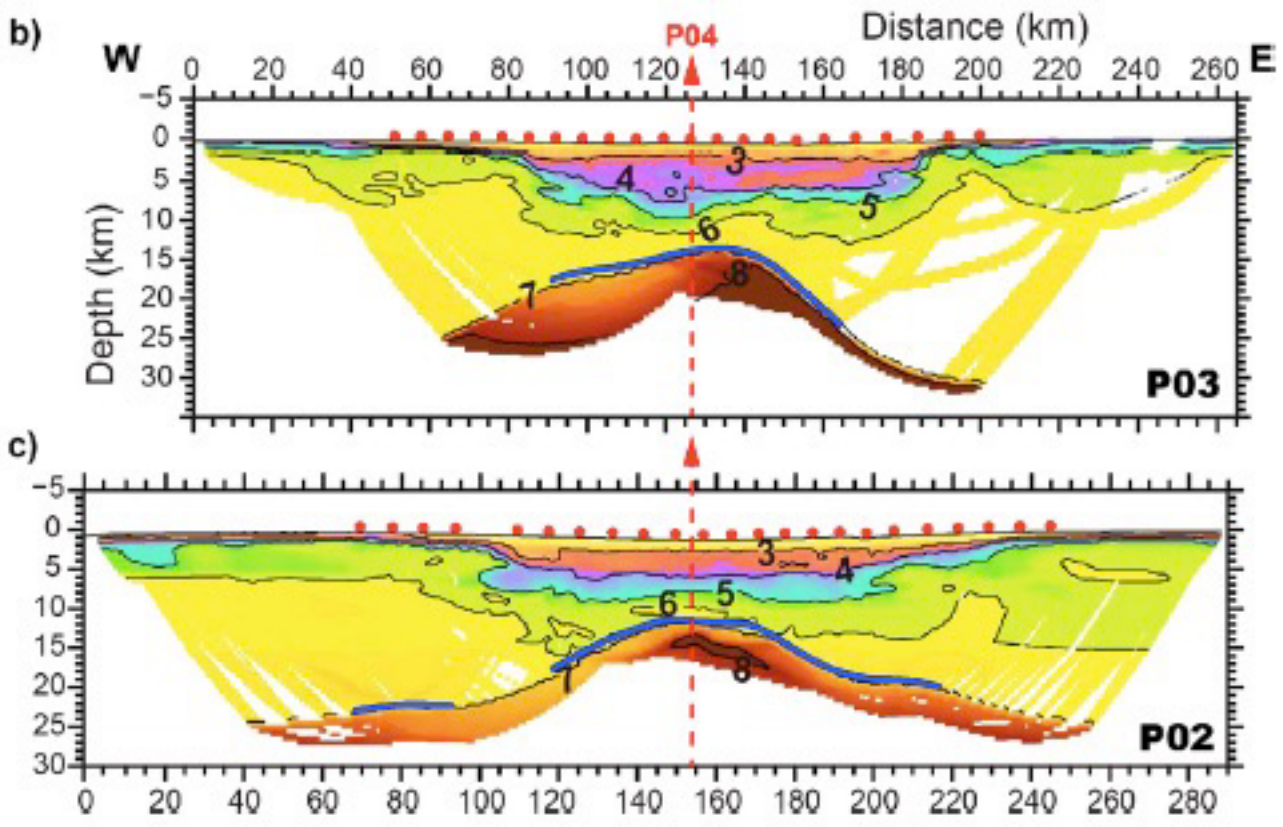

Prada M, Watremez L, Chen C, et al. Crustal strain-dependent serpentinisation in the Porcupine Basin, offshore Ireland[J]. Earth and Planetary Science Letters, 2017, 474: 148-159.

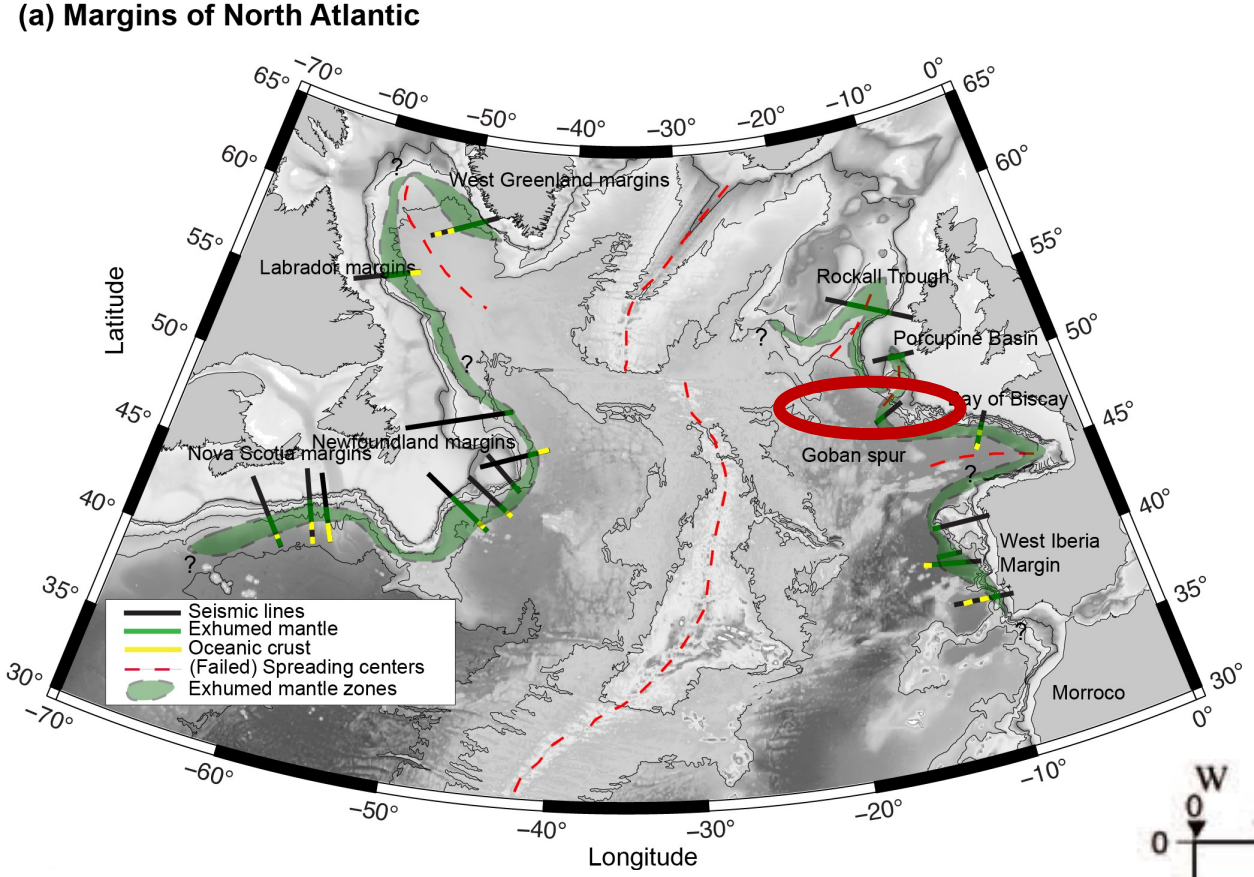

Goban spur

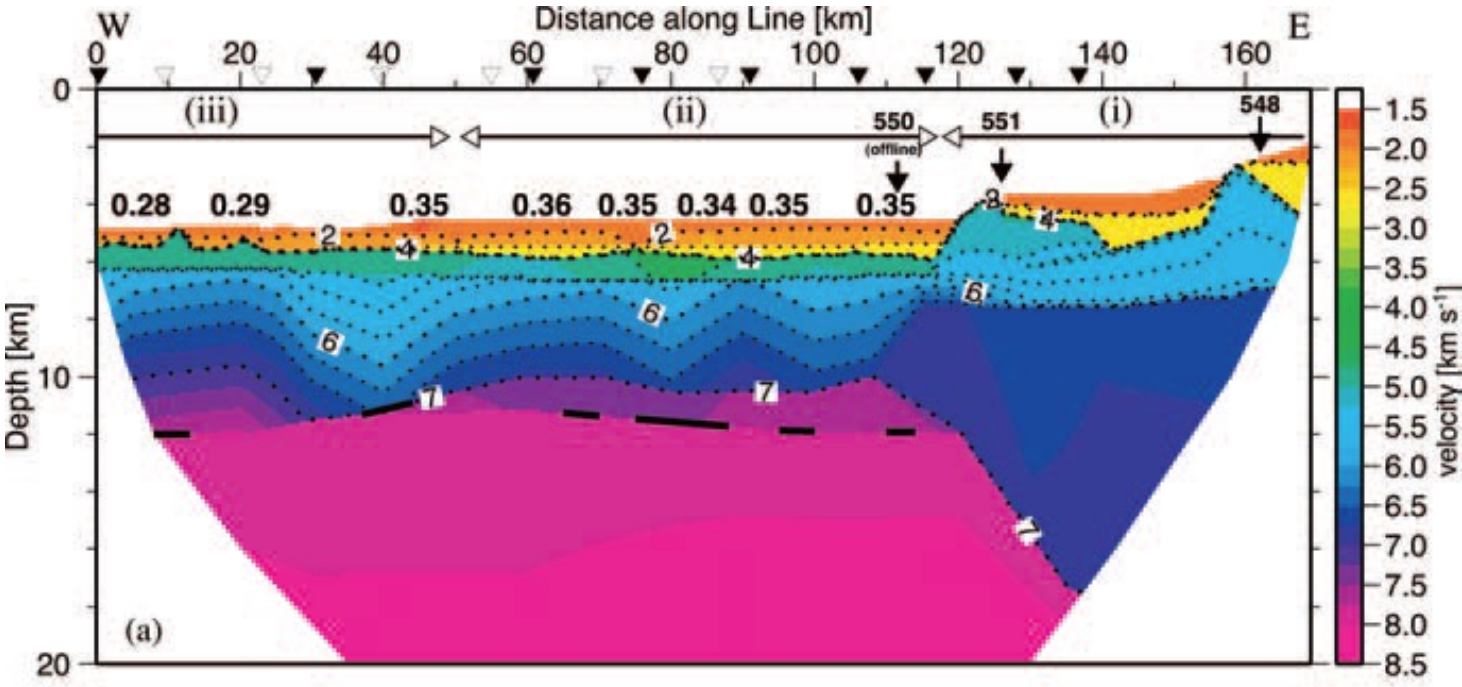

Bullock, A. D., and Minshull, T. A., 2005, From continental extension to seafloor spreading: crustal structure of the Goban Spur rifted margin, southwest of the UK: Geophysical Journal International, v. 163, no. 2, p. 527-546.

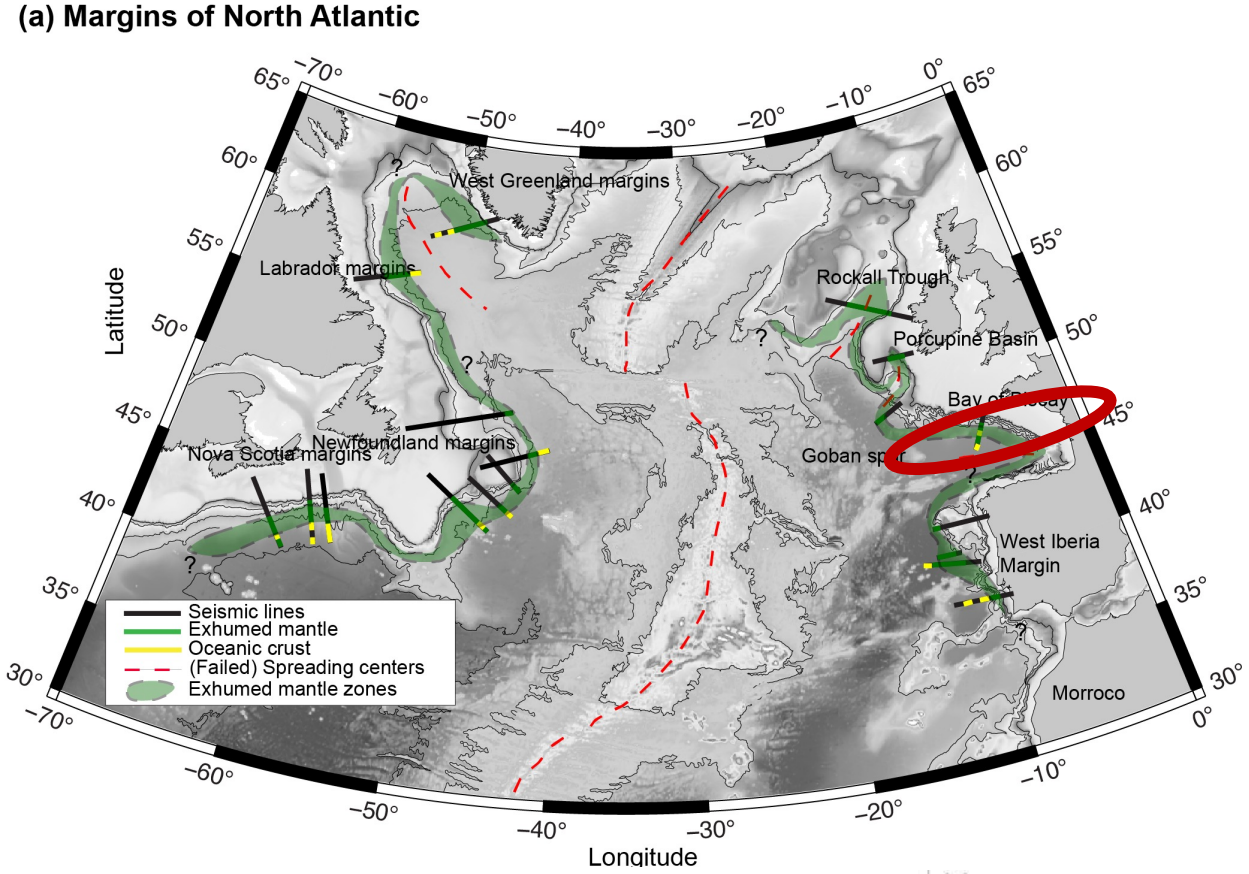

Bay of Biscay

Thinon, I., Matias, L., Réhault, J.-P., Hirn, A., Fidalgo-González, L., and Avedik, F., 2003, Deep structure of the Armorican Basin (Bay of Biscay): a review of Norgasis seismic reflection and refraction data: Journal of the Geological Society, v. 160, no. 1, p. 99-116.

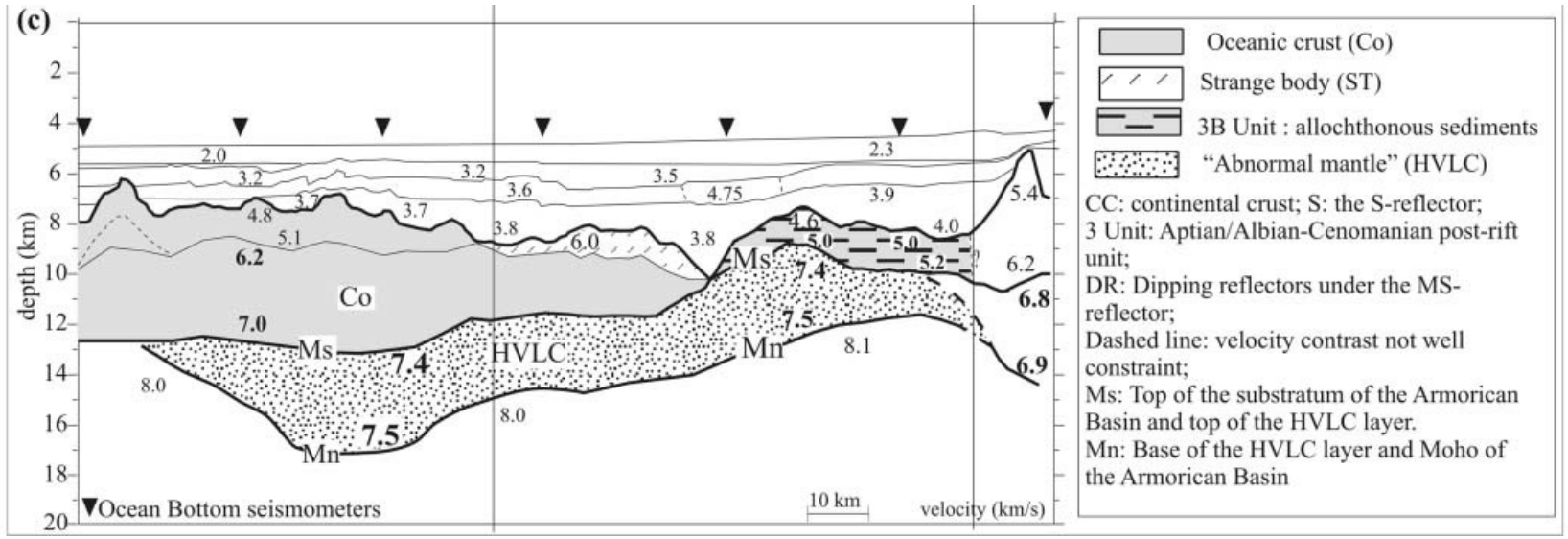

(a) Margins of North Atlantic

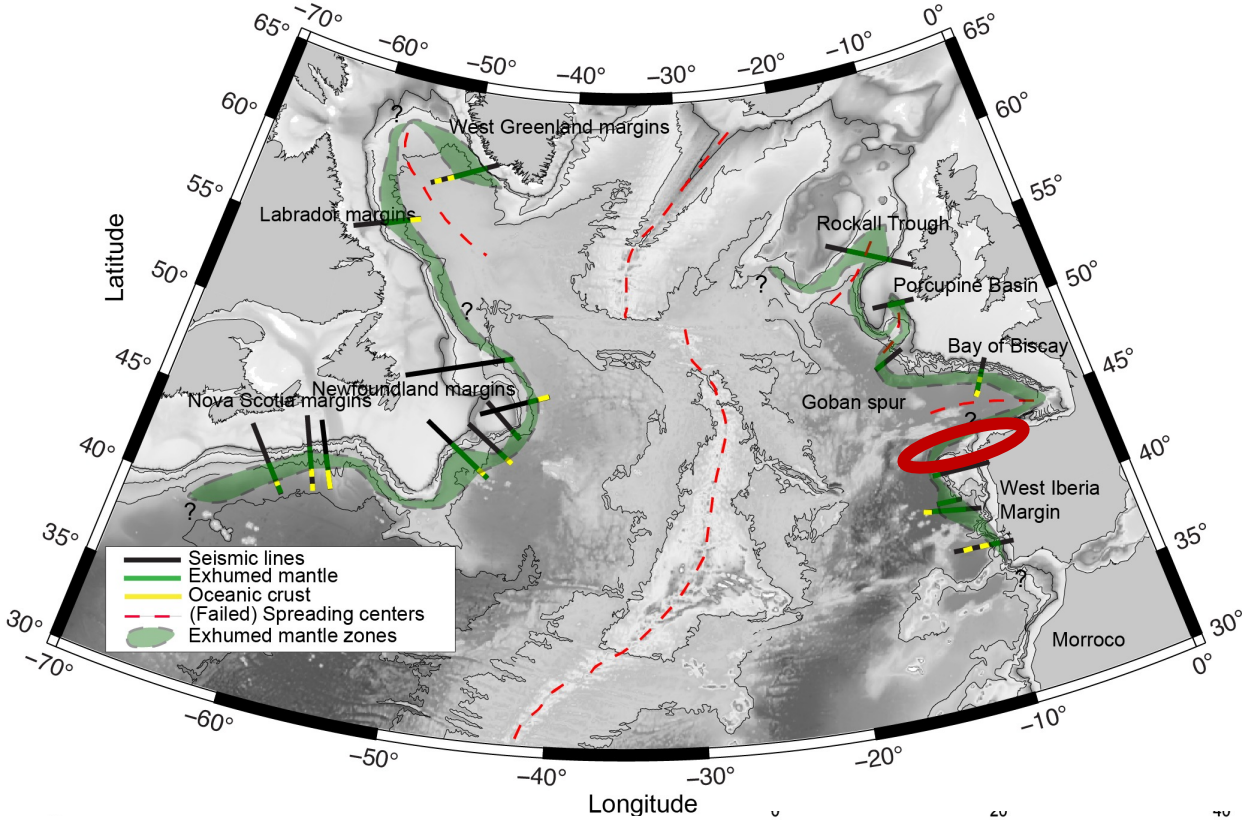

Northern WIM

Dean, S. L., Sawyer, D. S., and Morgan, J., 2015, Galicia Bank ocean–continent transition zone: New seismic reflection constraints: Earth and Planetary Science Letters, v. 413, p. 197-207.

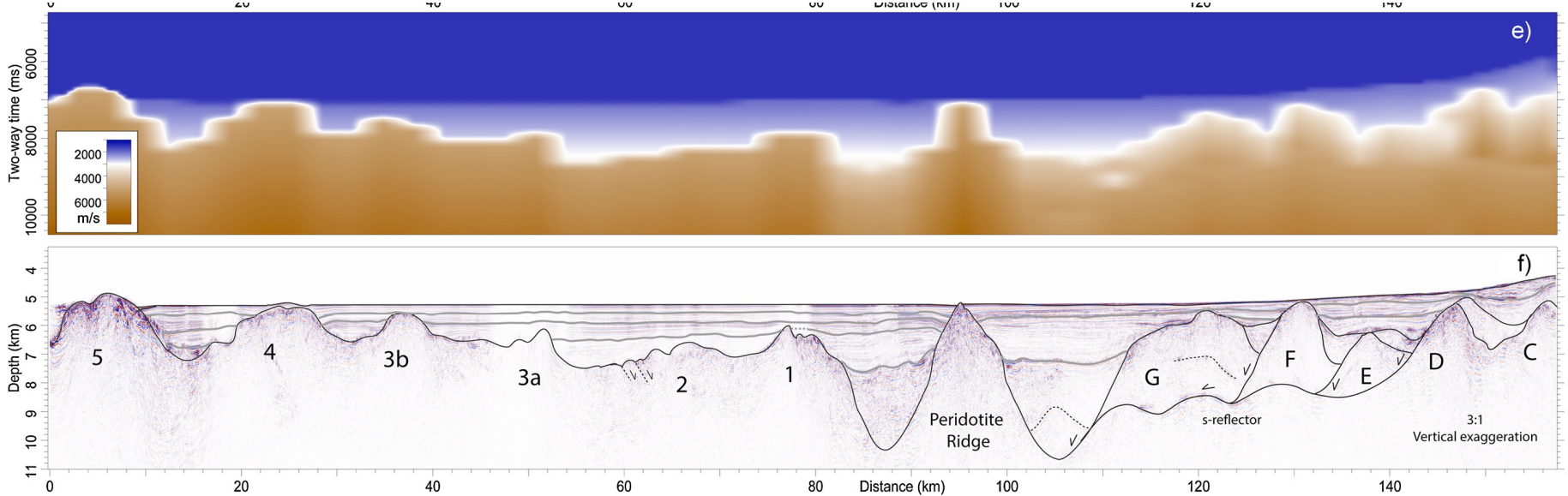

(a) Margins of North Atlantic

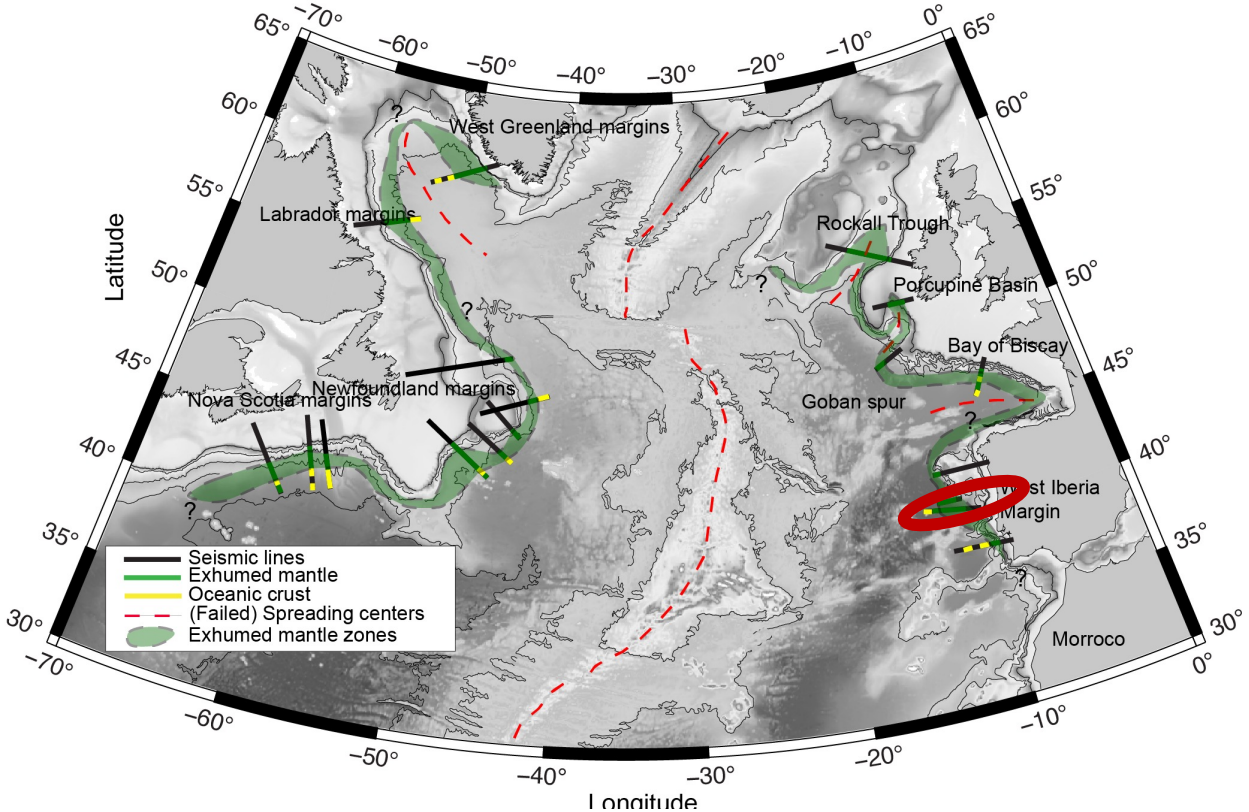

Central WIM

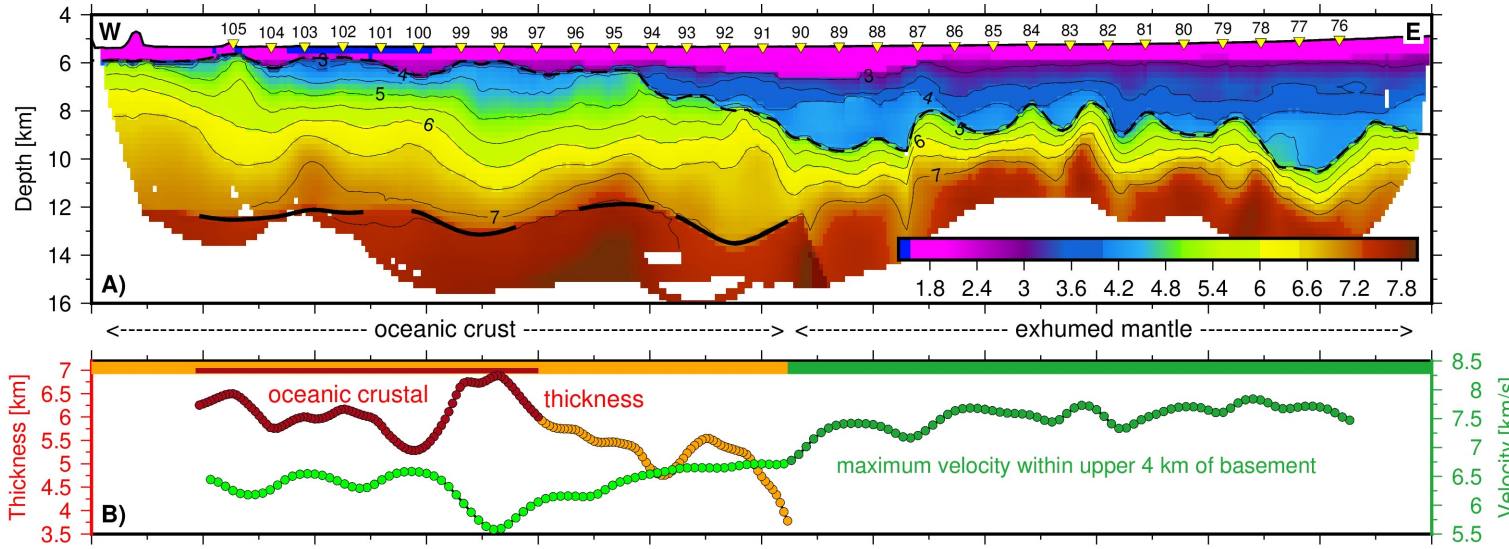

Grevemeyer, I., Ranero, C. R., Papenberg, C., Sallares, V., Bartolomé, R., Prada, M., Batista, L., and Neres, M., 2022, The continent-to-ocean transition in the Iberia Abyssal Plain: Geology doi: https://doi.org/10.1130/G49753.1.

(a) Margins of North Atlantic

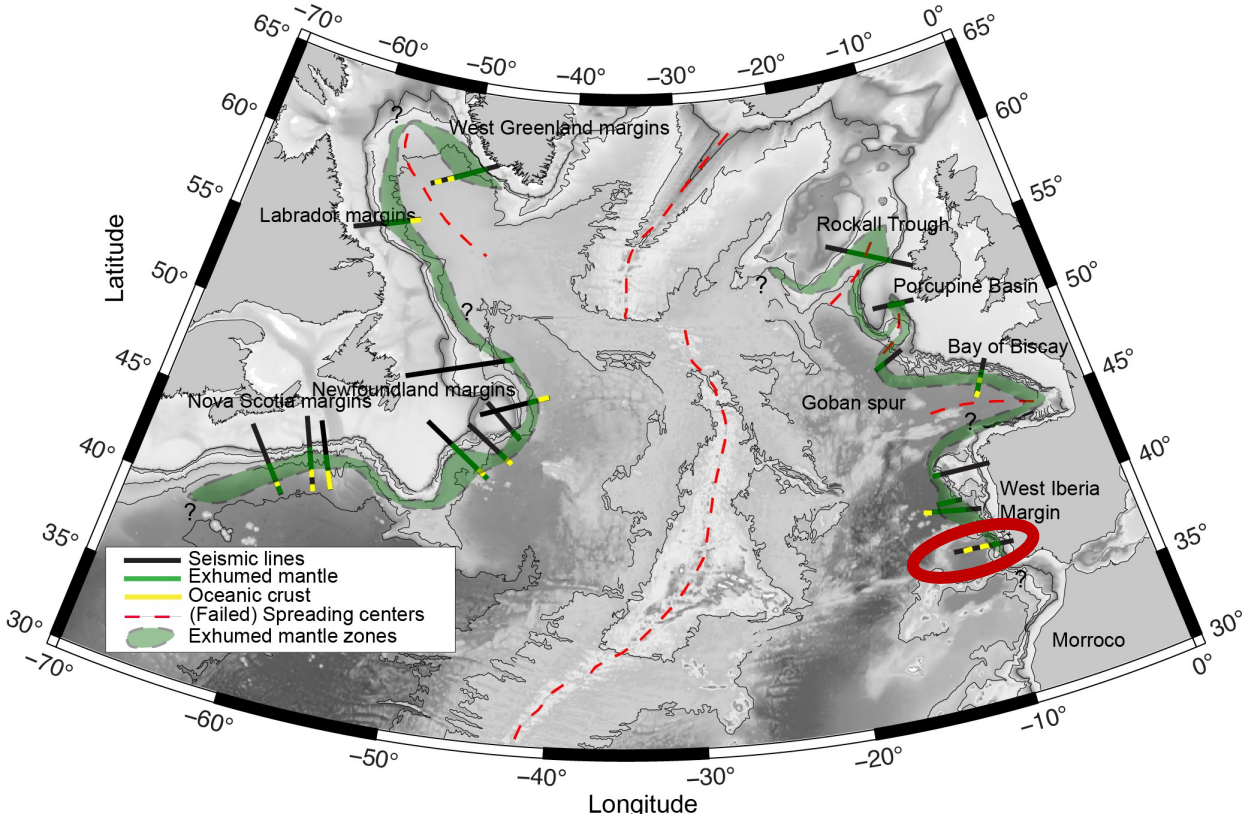

Southern WIM

Merino, I., Ranero, C. R., Prada, M., Sallarès, V., and Grevemeyer, I., 2021, The Rift and Continent‐Ocean Transition Structure Under the Tagus Abyssal Plain West of the Iberia: Journal of Geophysical Research: Solid Earth, v. 126, no. 11, p. e2021JB022629.